metals

MDPI

Article

Stress Corrosion Cracking Mechanisms of UNS S32205 Duplex Stainless Steel in Carbonated Solution Induced by Chlorides

Ulises Martin and David M. Bastidas *

National Center for Education and Research on Corrosion and Materials Performance, NCERCAMP-UA, Department of Chemical, Biomolecular, and Corrosion Engineering, The University of Akron, 302 E Buchtel Ave, Akron, OH 44325-3906, USA

* Correspondence: dbastidas@uakron.edu; Tel.: +1-330-972-2968

Abstract: Herein, the chloride-induced stress corrosion cracking (SCC) mechanisms of UNS S32205 duplex stainless steel (DSS) reinforcing bars in alkaline and carbonated solutions are studied. Electrochemical monitoring and mechanical properties were tested using linear polarization resistance and electrochemical impedance spectroscopy, coupled with the slow strain rate tensile test (SSRT) to evaluate the SCC behavior and unravel the pit-to-crack mechanisms. Pit initiation and crack morphology were identified by fractographic analysis, which revealed the transgranular (TG) SCC mechanism. HCO_3^- acidification enhanced the anodic dissolution kinetics, thus promoting a premature pit-to-crack transition, seen by the decrease in the maximum phase angle in the Bode plot at low frequencies (≈ 1 Hz) for the carbonated solution. The crack propagation rate for the carbonated solution increased by over 100% compared to the alkaline solution, coinciding with the lower phase angle from the Bode plots, as well as with the lower charge transfer resistance. Pit initiation was found at the TiN nonmetallic inclusion inside the ferrite phase cleavage facet, which developed TG-SCC.

Keywords: stress corrosion cracking (SCC); pit-to-crack mechanism; electrochemical impedance spectroscopy (EIS); fractographic study; crack propagation

Citation: Martin, U.; Bastidas, D.M. Stress Corrosion Cracking Mechanisms of UNS S32205 Duplex Stainless Steel in Carbonated Solution Induced by Chlorides. *Metals* **2023**, *13*, 567. https://doi.org/10.3390/met13030567

Academic Editor: Tiziano Bellezze

Received: 25 January 2023
Revised: 7 March 2023
Accepted: 10 March 2023
Published: 11 March 2023

1. Introduction

Duplex stainless steel (DSS) has an outstanding combination of mechanical and corrosion properties thanks to its duplex microstructure consisting of a balanced ratio of ferrite (α–phase) and austenite (γ–phase), making this type of alloy widely employed in many industries [1]. The duplex microstructure comprises a banded structure with discontinuous island-like austenite grains embedded in a ferrite matrix [2]. Among the different varieties of DSS, the most commonly used is 2205 DSS, which has been applied for offshore construction and platforms in recent decades [3]. The superior corrosion resistance over austenitic stainless steel makes 2205 DSS a valuable option for harsh environments [4,5].

However, when a corrosive environment is linked with external loading, stress corrosion cracking (SCC) can be developed, threatening the service lifetime of structural materials in marine environments [6]. For this reason, the corrosion and SCC behavior of DSS have been widely studied in the literature. In the case of chloride electrolyte, the preferential phase to dissolve is the α–phase until a threshold chloride concentration is reached (0.1 M NaCl at pH 3 and 60 °C), promoting lacy cover pitting instead in both phases [7,8]. Another focus of previous studies was on the property mismatch between phases such as the mechanical phase, where the α–phase cannot develop as high tensile stresses as the γ–phase [9], and the electrochemical phase, where the α–phase has lower corrosion potential (E_{corr}) (higher corrosion susceptibility) [10], also leading to galvanic microcouples [11]. Even in hydrogen diffusion, the interstitial voids of the α–phase crystal structure allow for more hydrogen trapping [12]. When SCC is triggered in DSS, the crack

is preferentially nucleated in the α–phase, propagating transgranularly and promoting brittle fracture, while the γ–phase usually fails by ductile tearing and acts as a physical barrier for the crack propagation. Two main mechanisms are accepted for the failure of DSS in marine environments: anodic dissolution (AD) and hydrogen embrittlement (HE). Nevertheless, in cavities and inhomogeneities such as the pit bottom or the tip of the crack, localized acidification can occur, triggering a mix of both AD and HE [13]. In the case of AD, inhomogeneous microstructures such as the heat-affected zone are more likely to promote it [14].

When subjected to a carbonated environment, the corrosion performance is affected, thus also promoting changes in the SCC behavior [15]. An SCC study on 2205 DSS subjected to a H_2S–CO_2 environment revealed that at low pH, the anodic current density increased due to additional hydrogen ions generated during the dissociation of H_2CO_3, and that the presence of CO_2 did not affect the SCC development [16]. When the pH was higher, the presence of CO_2 played a relevant role in the SCC behavior promoting AD. In a different work, the critical chloride concentration of stainless steel (SS) reinforcements and its dependence on carbonation was studied, and it was found that the critical chloride concentration decreases when the temperature is increased [17]. Comparing the chloride-induced corrosion resistance of SS in alkaline and carbonated concrete solutions, it was found that for carbonated solutions, the SS corrosion resistance was reduced [18].

Nevertheless, there is still a lack of knowledge on the SCC mechanism of DSS immersed in alkaline environments contaminated with chlorides and the influence of the carbonation process. For that reason, this study seeks to unravel the SCC mechanism and the pit-to-crack transition of UNS S32205 reinforcements in chloride-contaminated alkaline and carbonated solutions. To measure the change in the mechanical and electrochemical properties, a combination of the slow strain rate test (SSRT) with continuous monitoring of electrochemical properties by the linear polarization resistance (LPR) technique, as well as electrochemical impedance spectroscopy (EIS), is presented. Fractographic study of the post-mortem specimens is correlated with the crack propagation rates and the electrochemical analysis.

2. Materials and Methods

2.1. Materials

The UNS S32205 reinforcing bars were 10 mm in diameter (size #3). The elemental composition of UNS S32205 (DSS 2205) reinforcing steel is shown in Table 1. The specimens were machined with a circular 60° V–notch in the center of the sample to accelerate the crack initiation process during the SSRT. Before the testing, samples were rinsed with deionized (DI) water, degreased with acetone, and blow-dried with air. A 3 cm^2 exposed area was selected by coating with epoxy lacquer (Midas 335-009 nonconductive paint). The samples were epoxy mounted and polished to mirror finishing by SiC paper and diamond powder (1 μm) for microstructural characterization. The etchant solution used to reveal the microstructure contained 40 wt.% NaOH, samples were exposed for 5 s to an applied potential of 3 V. The metallographic study was performed using scanning electron microscopy (SEM) in a Tescan Lyra 3 XMU. Finally, X-ray diffraction (XRD) analysis was performed using a Rigaku SmartLab-3kW X-ray diffractometer, with a Cu target (K_α = 1.5406 Å), and a scan step of 2°/min over the 2θ range of 40°–95°.

Table 1. Elemental composition of UNS S32205 (DSS 2205) reinforcing bar (wt.%), Fe balance.

Element	C	Cr	Mn	Ni	Mo	N	Si	Co	Ti
Content (wt.%)	0.017	22.76	1.57	4.64	3.21	0.171	0.34	0.17	0.004

2.2. Testing Method and Environment

UNS S32205 reinforcement specimens were tested under SCC conditions via uniaxial tensile test by the SSRT while being immersed in corrosive media following ASTM-

G129 [19]. The SSRT experiments were conducted with a strain rate of 1×10^{-6} s^{-1} to increase the number of environmental interactions. The electrochemical tests conducted during the straining of the sample were performed using a three-electrode configuration cell setup with a Gamry potentiostat Series 600. The reference electrode (RE) used in this test was a saturated calomel electrode (SCE), a graphite rod as the counter electrode (CE), and the UNS S32205 specimen as the working electrode (WE). Three different chloride concentrations were tested 0, 4, and 8 wt.% of Cl^- by means of $CaCl_2$ additions. These chlorides concentrations were selected based on the chloride threshold of stainless steel in reinforced concrete (4.9 wt.% Cl^-), thus 4 wt.% Cl^- is below the value, and 8 wt.% Cl^- is above it, highlighting the effect of the chloride content on the development of SCC [20].

The simulated concrete pore solution (SCPS) was made out of saturated $Ca(OH)_2$ aqueous solution (pH 12.6). Additionally, a carbonated buffer solution (CBS) was prepared by a carbonate/bicarbonate solution (pH 9.1), mixing 0.01 M Na_2CO_3 and 0.1 M $NaHCO_3$ aqueous solutions. The electrochemical testing was recorded after a steady-state open-circuit potential (OCP) value was reached over the period of 1 h. First, during the straining electrode test, linear polarization resistance (LPR) measurements were recorded with an applied potential scan range of ± 15 mV_{OCP} at a scan rate of 0.1667 mV s^{-1}, according to ASTM G59-97 [21]. Then, EIS measurements were recorded at the OCP, in a frequency range of 10^5–10^{-1} Hz with an applied 10 mV AC excitation signal and at a step rate of 10 points per decade. This set of experiments was repeated every hour. The SSRT was not put on hold during the measurements of the EIS and LPR to avoid unwanted creep. All tests were performed in triplicate to ensure reproducibility.

2.3. Characterization Techniques

The surface morphology of specimens was studied via scanning electron microscopy (SEM). The SEM analysis was performed in secondary electron mode (SE) at an accelerating voltage of 15 kV and at a working distance of 10 mm. In addition, local compositional analysis was obtained by the energy-dispersive X-ray spectroscopy (EDX) technique.

3. Results

3.1. Microstructure Characterization

The microstructure of the UNS S32205 reinforcement in the rolling direction can be seen in Figure 1a, where the γ–phase grains have a lamellar structure and are embedded in the α–phase matrix [22]. This microstructure has the γ–phase grains isolated in the α–phase matrix (with an α/γ interface), presenting a dispersed structure [23].

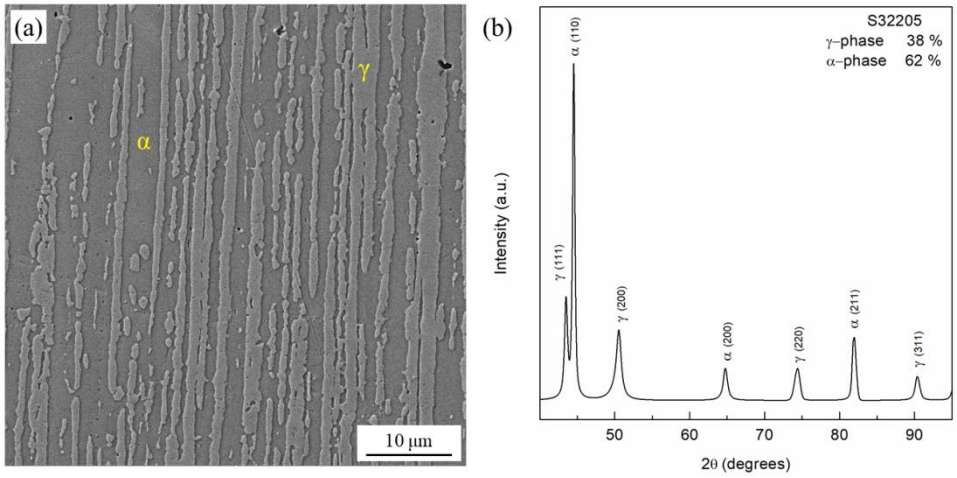

Figure 1. Microstructural characterization of as-received UNS S32205 reinforcement: (**a**) micrograph of the rolling direction ×50, and (**b**) XRD pattern and alloy phase fraction (γ–phase and α–phase).

Figure 1b depicts the X-ray diffraction pattern, where the diffraction peaks were composed of a body-centered cubic (BCC) α–phase (JCPDS No. 06-0694) and a face-centered cubic (FCC) γ–phase (JCPDS No. 33-0397) [24,25]. The ratio of the α–/γ–phases was quantified by the integration of the intensity peaks of the respective phases giving 62% for the α–phase and 38% for the γ–phase.

3.2. Slow Strain Rate Test (SSRT)

The stress/strain curves of the UNS S32205 reinforcement immersed in both electrolyte solutions, SCPS and CBS, under the three chloride concentrations can be seen in Figure 2. The mechanical behavior with the different chloride additions barely changed between pHs, having similar yield strength (σ_y) and ultimate tensile strength (σ_{UTS}). However, both the elongation to σ_{UTS} (ε_{UTS}) and the final elongation to failure (ε_f) were reduced (see Table 2).

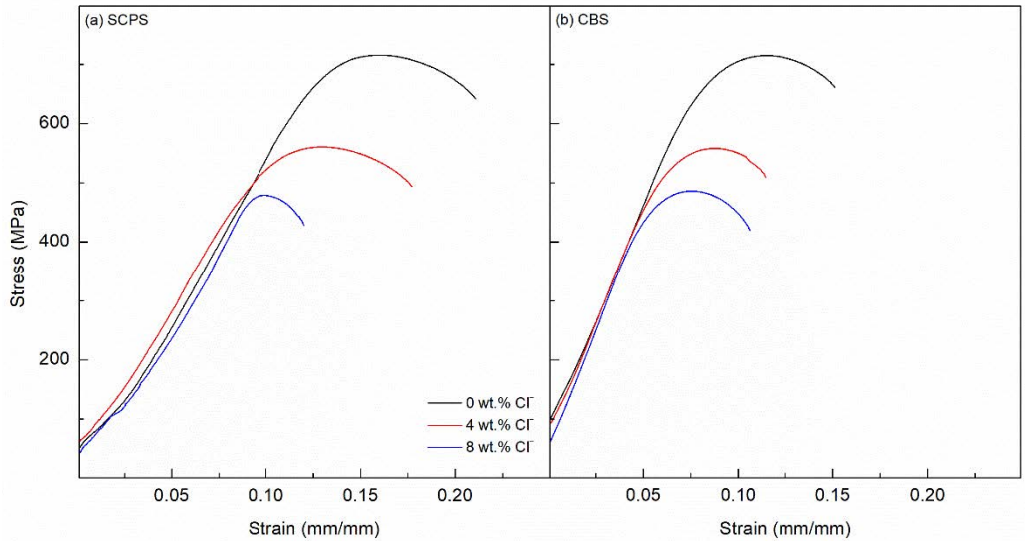

Figure 2. Stress/strain curves of UNS S32205 reinforcement as a function of the chloride content: (**a**) simulated concrete pore solution (SCPS, pH 12.6), and (**b**) carbonated solution (CBS, pH 9.1).

Table 2. Mechanical properties of UNS S32205 reinforcement after slow strain rate test (SSRT) in simulated concrete pore solution (SCPS, pH 12.6), and carbonated (CBS, pH 9.1) environments at different chloride concentrations.

$[Cl^-]$ wt.%	σ_y MPa	σ_{UTS} MPa	ε_{UTS} %	ε_f %
SCPS (pH 12.6)				
0	510	717	15.9	21.0
4	463	562	12.8	17.6
8	407	480	9.9	11.9
CBS (pH 9.1)				
0	512	716	11.7	15.1
4	461	559	8.9	11.5
8	406	485	7.7	10.5

The pH acidification due to the CO_2 formation in the aqueous solution yields carbonic acid (H_2CO_3), which later dissociates into HCO_3^- and CO_3^{2-} [26]. Then, by recombination with the Fe^{2+} cations in the solution, the formation of $FeCO_3$ is promoted, which subsequently dissolves and promotes further local acidification by the presence of H^+ [27]. This enhanced iron acid hydrolysis is responsible for the reduction of the mechanical properties [28]. The dissolution of the metal surface will release Fe^{3+} ions, which will combine

with the Cl^- in the solution and form $FeCl_3$, then its dissociation will increase the local acidification, acting as an autocatalytic process [28,29].

3.3. Linear Polarization Resistance (LPR)

LPR was used to monitor the corrosion current density (i_{corr}) during the SSRT, which was calculated using the Stern–Geary relationship, $i_{corr} = B/R_p$, where R_p is the polarization resistance, and B is the Stern–Geary constant (B = 26 mV [30]). However, the i_{corr} values had to be compensated due to the ohmic drop effect of the electrolyte, as the measured R_p from the LPR also included them [31]. In order to correct it, the EIS technique was used to find the resistance of the electrolyte (R_s) and subtract it from the R_p. Figure 3 shows the combined monitoring of the corrosion potential (E_{corr}) and the i_{corr} for the UNS S32205 reinforcement immersed in both the SCPS and the CBS under the three chloride concentrations.

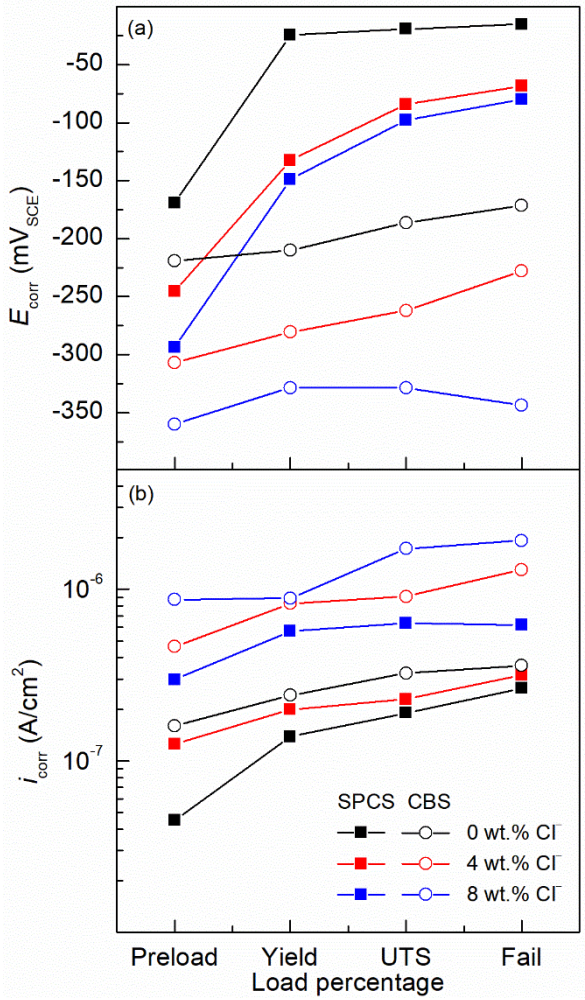

Figure 3. Linear polarization resistance measurements of UNS S32205 reinforcement during slow strain rate test (SSRT): (**a**) E_{corr}, and (**b**) i_{corr}.

The samples immersed in the SCPS experienced ennoblement in the E_{corr} with immersion time, increasing their value from the "Preload" up to the "Failure" (the load percentage "Failure" denotes the last measurement before the failure of the sample under SSRT). In addition, the higher the chloride concentration, the lower the E_{corr} value, corresponding to higher chloride susceptibility. The 0 wt.% Cl^- stabilized its E_{corr} at −25 mV_{SCE}, while both 4 and 8 wt.% Cl^- stabilized around −80 mV_{SCE}. Accordingly, the more the i_{corr} was lowered, the nobler the E_{corr} was, with the SCPS with lower chloride content having the

lowest values. The i_{corr} values for the SCPS were below 1 μA/cm^2, denoting low corrosion rate [30].

The CBS showed more cathodic values for the E_{corr} than their counterpart, exhibiting higher susceptibility to the aggressive environment due to the lower pH. The starting E_{corr} values for the CBS were more cathodic, stabilizing at −170, −230, and −330 mV_{SCE} for 0, 4, and 8 wt.% Cl^-, respectively. Coinciding with the active E_{corr} values, the i_{corr} values were also higher than the SCPS, with the CBS without chlorides having close i_{corr} values to the SCPS with 4 wt.% Cl^-. The CBS with 4 wt.% Cl^- content reached 1 μA/cm^2 at "Failure", while the 8 wt.% Cl^- surpassed it at the UTS.

3.4. Electrochemical Impedance Spectroscopy (EIS)

EIS analysis was performed for the UNS S32205 reinforcement during the different loading percentages for both pHs to study the passive film/steel interface. The Nyquist plots for both solutions can be seen in Figure 4 (SCPS Figure 4a–c and CBS Figure 4d–f), where a decreasing impedance trend with increasing chloride content is shown, coinciding with the behavior from the LPR analysis. In addition, the samples exposed to the CBS had lower impedances than the SCPS, which was attributed to the more acidic environment. However, the impedance decrease was not substantial as it did not reduce by an order of magnitude.

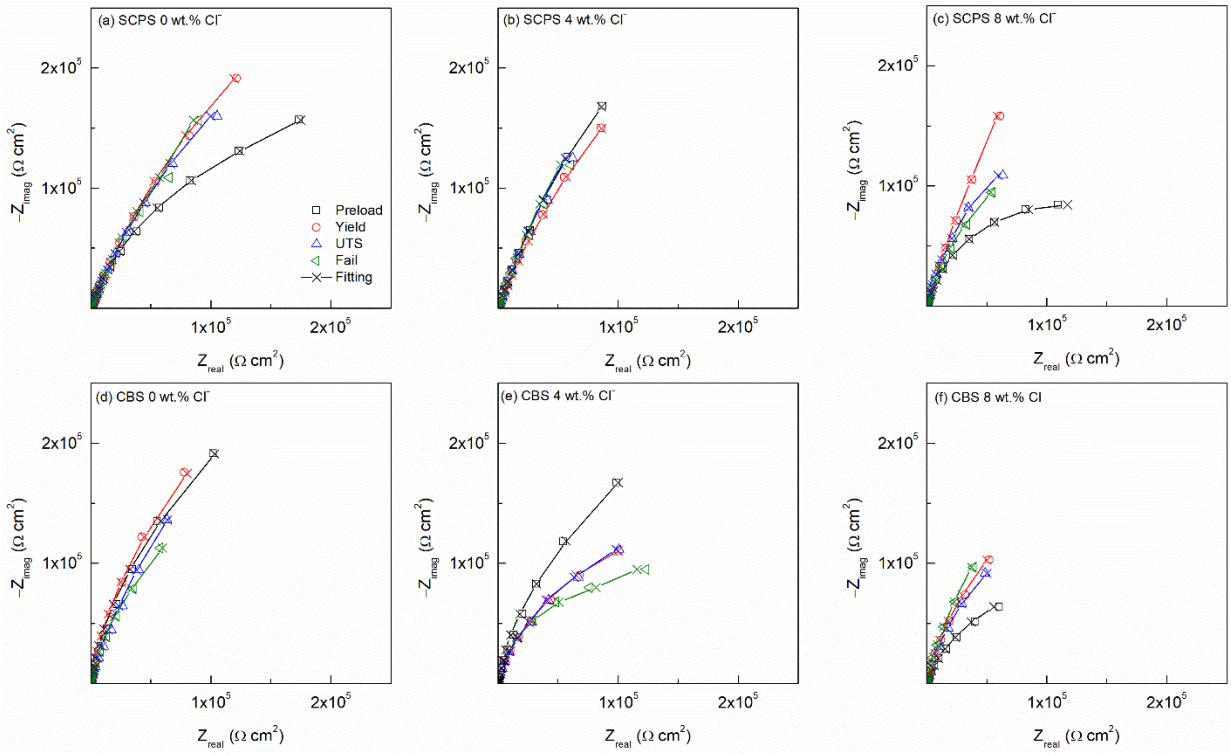

Figure 4. Nyquist plots of UNS S32205 reinforcement during slow strain rate test (SSRT): (**a**) SCPS 0 wt.% Cl^-, (**b**) SCPS 4 wt.% Cl^-, (**c**) SCPS 8 wt.% Cl^-, (**d**) CBS 0 wt.% Cl^-, (**e**) CBS 4 wt.% Cl^-, and (**f**) CBS 8 wt.% Cl^-.

Furthermore, the EIS data were fitted to a hierarchically distributed electric equivalent circuit (EEC) with two time constants to analyze the passive film/steel interface (see Figure 5) [32,33]. The elements of the EEC represent the resistance of the electrolyte solution (R_s), the first time constant ($R_{film}//CPE_{film}$) representing the passive film on the UNS S32205 reinforcement surface, found at high frequency, where R_{film} and CPE_{film} are the parameters defining the passive film; and the second time constant ($R_{ct}//CPE_{dl}$), defining the corrosion process and attributed to low-frequency processes, where R_{ct} and CPE_{dl} define the charge transfer resistance and the electrochemical double-layer capacitance. The

fitting parameters of the proposed EEC for each of the tested solutions are seen in Table 3, where an average chi-square (χ^2) of 10^{-3} and a total error for each element less than 10% were obtained.

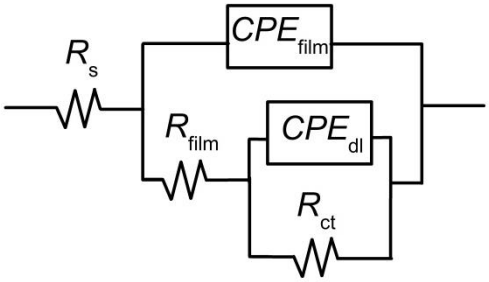

Figure 5. Electric equivalent circuit (EEC) with two time constants.

Table 3. Fitting EIS parameters for UNS S32205 reinforcement during slow strain rate test (SSRT) for SCPS and CBS.

[Cl⁻] wt.%	Load Percentage	R_s	R_{film}	Y_{film}	n_{film}	R_{ct}	Y_{dl}	n_{dl}	χ^2 (*)
		Ω cm²	Ω cm²	S cm^{-2} s^{n,film}		Ω cm²	S cm^{-2} s^{n,dl}		
SCPS (pH 12.6)									
0	Preload	3.82	8.75×10^2	1.26×10^{-6}	0.81	4.29×10^5	2.19×10^{-6}	0.84	8.87×10^{-4}
	Yield	3.61	4.25×10^3	1.60×10^{-6}	0.94	9.03×10^5	2.82×10^{-6}	0.85	3.77×10^{-3}
	UTS	3.75	3.55×10^3	1.33×10^{-6}	0.93	1.08×10^5	3.03×10^{-6}	0.86	3.84×10^{-3}
	Failure	3.85	3.45×10^3	4.41×10^{-6}	0.92	1.06×10^5	3.83×10^{-6}	0.86	8.11×10^{-4}
4	Preload	3.82	2.54×10^3	2.19×10^{-6}	0.89	7.77×10^5	1.43×10^{-6}	0.98	2.69×10^{-3}
	Yield	3.98	3.26×10^3	3.16×10^{-6}	0.87	1.49×10^5	2.65×10^{-6}	0.87	2.61×10^{-3}
	UTS	3.91	2.59×10^3	3.74×10^{-6}	0.86	1.68×10^5	3.42×10^{-6}	0.87	2.91×10^{-3}
	Failure	3.90	2.57×10^3	4.18×10^{-6}	0.86	1.75×10^5	4.57×10^{-6}	0.89	3.52×10^{-3}
8	Preload	3.78	1.44×10^3	4.05×10^{-6}	0.81	7.85×10^4	3.05×10^{-6}	0.89	7.64×10^{-4}
	Yield	3.96	2.08×10^3	6.08×10^{-6}	0.83	1.78×10^5	4.18×10^{-6}	0.89	2.75×10^{-3}
	UTS	3.88	1.09×10^3	6.35×10^{-6}	0.86	1.24×10^5	4.95×10^{-6}	0.88	2.67×10^{-3}
	Failure	3.95	1.01×10^3	8.85×10^{-6}	0.83	6.04×10^4	5.28×10^{-6}	0.79	1.40×10^{-3}
CBS (pH 9.1)									
0	Preload	3.77	2.57×10^3	1.91×10^{-6}	0.91	4.10×10^5	1.87×10^{-6}	0.78	4.68×10^{-4}
	Yield	3.59	1.34×10^3	2.14×10^{-6}	0.95	2.01×10^5	4.68×10^{-6}	0.73	4.91×10^{-4}
	UTS	3.81	1.21×10^3	4.07×10^{-6}	0.95	2.47×10^5	5.56×10^{-6}	0.73	4.21×10^{-4}
	Failure	3.82	1.87×10^3	4.96×10^{-6}	0.97	3.22×10^5	5.55×10^{-6}	0.72	6.57×10^{-4}
4	Preload	3.61	1.94×10^3	5.33×10^{-6}	0.86	1.28×10^5	1.23×10^{-6}	0.77	1.39×10^{-3}
	Yield	3.84	1.16×10^3	6.06×10^{-6}	0.83	2.82×10^5	2.86×10^{-6}	0.74	2.03×10^{-3}
	UTS	3.85	1.01×10^3	6.82×10^{-6}	0.86	2.79×10^5	4.90×10^{-6}	0.75	2.09×10^{-3}
	Failure	3.71	8.61×10^2	7.91×10^{-6}	0.78	7.35×10^4	5.14×10^{-6}	0.74	1.85×10^{-3}
8	Preload	3.72	1.73×10^3	1.31×10^{-6}	0.84	1.58×10^4	2.95×10^{-6}	0.81	8.21×10^{-4}
	Yield	3.99	7.38×10^2	5.92×10^{-6}	0.81	1.34×10^4	5.40×10^{-6}	0.71	5.18×10^{-4}
	UTS	3.98	5.43×10^2	7.63×10^{-6}	0.88	2.99×10^4	6.44×10^{-6}	0.74	1.18×10^{-3}
	Failure	3.91	3.91×10^2	8.24×10^{-6}	0.87	1.60×10^4	6.25×10^{-6}	0.73	9.54×10^{-4}

* Total Error < 10% for all values.

Before the fitting of the EIS data was analyzed by the proposed EEC, Kramers–Kronig transformations were performed to prove the robustness of the experimental data (see Equations (1) and (2)) [34]:

$$Z_{\mathrm{Real}}(\omega) = Z_{\mathrm{Real}}(\infty) - \frac{2}{\pi}\int_0^{\infty} \frac{x\, Z_{\mathrm{Imag}}(x) - \omega\, Z_{\mathrm{Imag}}(\omega)}{x^2 - \omega^2} dx \quad (1)$$

$$Z_{\mathrm{Imag}}(\omega) = -\frac{2\omega}{\pi}\int_0^{\infty}\frac{x\,Z_{Real}(x) - Z_{\mathrm{Real}}(\omega)}{x^2-\omega^2}dx \quad (2)$$

Using Equation (1), the real component can be calculated from the imaginary component, and with Equation (2), the imaginary component can be calculated from the real component [35]. Performing this analysis, the impedance data proved to be robust.

3.5. Fractographic Study

The fractographic analysis of the UNS S32205 reinforcement for all pHs and chloride additions was performed by SEM to unravel the failure mechanism. Figure 6 gathers all the micrographs for the samples tested in the SCPS. Starting with the 0 wt.% Cl^-, the failure is purely ductile (see Figure 6a), with microvoids and coalescence of dimples mainly attributed to the ductile behavior of the γ–phase (see Figure 6b) and some minor ductile overload areas (see Figure 6c) [36]. The samples tested in 4 wt.% Cl^- (see Figure 6d) developed more ductile overload areas compared to the 0 wt.% Cl^- (see Figure 6e), in addition to showing brittle fracture inside the ferrite cleavage facets (α–phase), in the form of cracks in an inclusion (see Figure 6f) [37,38]. Finally, the 8 wt.% Cl^- (see Figure 6g) revealed greater cracks and ferrite cleavage facets (see Figure 6h), and the inclusions were found to be the sites for the crack nucleation (see Figure 6i) [10]. It could be seen that the cracks preferentially initiated in the ferrite cleavage facets and propagated along the phase boundaries, while the γ–phase deformed the microvoids at the grain boundaries (tearing ridges) [39].

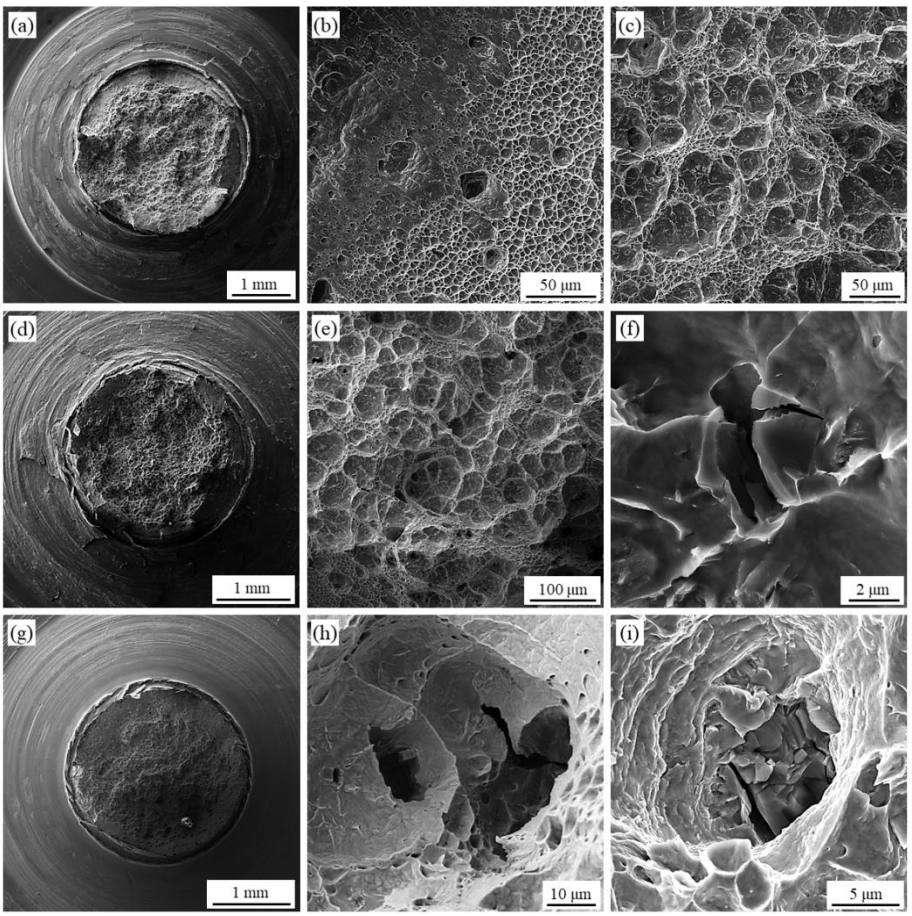

Figure 6. Micrographs of UNS S32205 reinforcement after slow strain rate test (SSRT) immersed in SCPS: 0 wt.% Cl^- (**a**) rupture surface ×50 (**b**) microvoids and coalescence of dimples ×1300, (**c**) ductile overload areas ×1000; 4 wt.% Cl^- (**d**) rupture surface ×50, (**e**) ductile overload area ×600, (**f**) brittle fracture inside the ferrite cleavage facets ×22,800 ; 8 wt.% Cl^- (**g**) rupture surface ×50, (**h**) cracks inside the ferrite cleavage facets ×4500, and (**i**) crack nucleation due to inclusions ×12,300.

The samples immersed in the CBS with 0 wt.% Cl^- also experienced a ductile fracture (see Figure 7a,b); however, by a mechanical stimulus, the inclusions were broken (see Figure 7c). The 4 wt.% Cl^- addition significantly changed the fracture mode (see Figure 7d), developing greater ferrite cleavage facets inside the ductile overload surface, a sign of a more brittle fracture mode (see Figure 7e) [9]. Increasing the magnifications inside the cleavage facets, microcracks were developed from side to side denoting transgranular SCC (TG-SCC) (see Figure 7f) [40]. The crack propagation is arrested at the grain boundary, coinciding with literature, where the γ/α interphase is known to avoid or change the crack propagation due to the lower cracking susceptibility of the γ–phase [9,41]. This is due to the lower required energy absorbed for the α–phase before cracking.

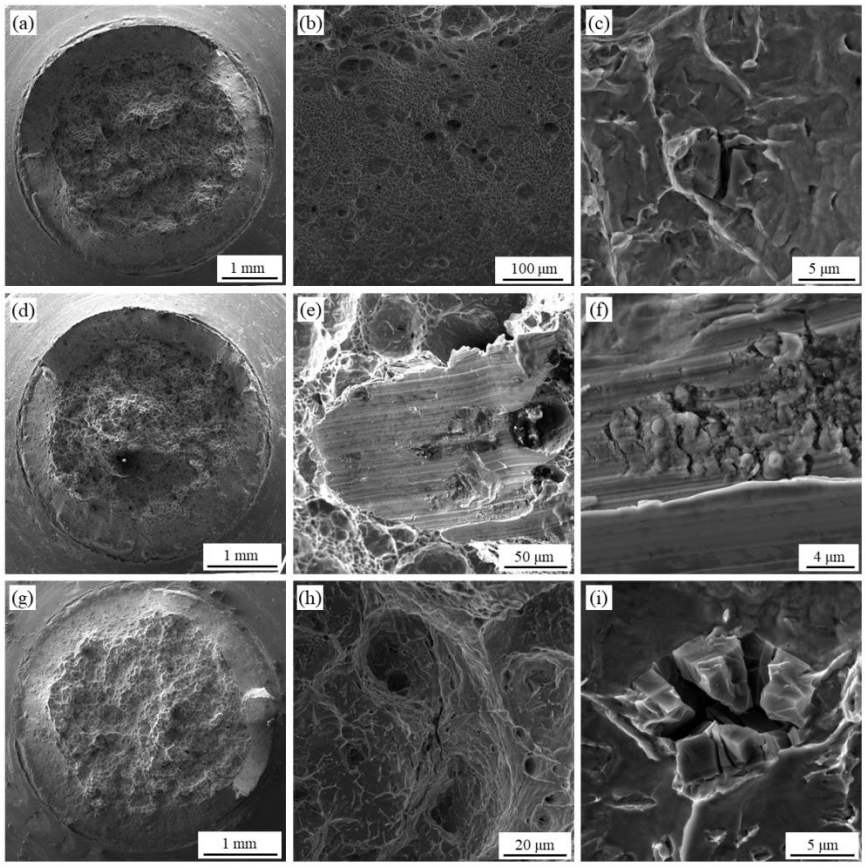

Figure 7. Micrographs of UNS S32205 reinforcement after slow strain rate test (SSRT) immersed in CBS: 0 wt.% Cl^- (**a**) rupture surface ×50 (**b**) microvoids and coalescence of dimples ×550, (**c**) broken inclusions ×11,200; 4 wt.% Cl^- (**d**) rupture surface ×50, (**e**) brittle fracture mode ×1200, (**f**) microcracks inside the ferrite cleavage facets ×10,300; 8 wt.% Cl^- (**g**) rupture surface ×50, (**h**) cracks inside the ferrite cleavage facets ×3100, and (**i**) crack nucleation due to inclusions ×7600.

The samples tested in 8 wt.% Cl^- were covered in cleavage facets, reducing the ductile overload areas, and inhibiting the formation of the cone shape, denoting even more brittle fracture (see Figure 7g). Figure 7h shows the formation of cracks inside the ferrite cleavage facets [37]. The low presence of ductile microvoids indicated that there was little tearing through γ–phase, supporting the idea of a more brittle α–phase coinciding with the higher density of cleavage facets [42]. As previously seen, the sites where the cracks nucleated were the inclusions, which appeared to be cracked in a brittle manner (see Figure 7i).

4. Discussion

4.1. Crack Propagation Rate

In order to correlate the effect of the carbonation process and the chloride content with the SCC susceptibility, the crack propagation rate (v_{crack}) was calculated based on the theoretical model proposed by Macdonald, which accommodates both electrochemical and mechanical properties (see Equation (3)) [43]. As the main element involved in the dissolution/cracking mechanism is the iron, all calculations will be based on it.

$$v_{crack} = \frac{M\, i_{corr}}{2\, \rho_m\, z\, F\, W\, \delta} \tag{3}$$

where ρ_m is the density of Fe (7.87 g cm^{-3}), F is Faraday's constant (96,487 C mol^{-1}), i_{corr} is the corrosion current density, M is the atomic weight of Fe, z is the oxidation state of the Fe dissolving at the crack tip, W is the specimen width, and δ is the crack tip opening distance.

The δ is related to the stress intensity factor (K_I) via Equation (4) [43]:

$$\delta = \frac{K_I^2(1-v^2)}{m\, \sigma_y\, E} \tag{4}$$

where v is the Poisson ratio, m is a constant, σ_y is the yield strength, and E is the modulus of elasticity.

The K_I for the circular sharp-V notch, with an angle between the walls of the notch equal to 60°, can be seen in Equation (5), where ρ is the radius of curvature, ω is a tabulated value, λ is the Williams' eigenvalue, and q is a real number ranging from 1.0 to 2.0 (flat edge to crack), and their values can be obtained following the work by Lazzarin and Filippi [44,45]:

$$K_I = \sigma \frac{\sqrt{2\pi}}{1+\omega} \left(\frac{q-1}{q}\rho\right)^{1-\lambda} \tag{5}$$

The K_I will increase until the critical K_I value where SCC is triggered (K_{ISCC}) is reached, which for UNS S32205, a $K_{ISCC} \approx 50$ MPa $\sqrt{m}$ will be assumed based on literature [46,47].

Figure 8 shows the v_{crack} and the stress as a function of time for SCPS (Figure 8a) and CBS (Figure 8b). The current density for the calculations was used from the LPR monitoring over the entire SSRT for the 4 and 8 wt.% Cl^- conditions. Once the K_{ISCC} is reached, the increase in current density makes for a rise in the v_{crack}. The samples strained in the SCPS once the K_{ISCC} was reached had a v_{crack} of 1.32 and 1.72 × 10^{-9} m/s for 4 and 8 wt.% Cl^-, respectively (see Figure 8a). After the plateau found at the K_{ISCC}, which is attributed to the crack nucleation time, the v_{crack} increases until the failure of the sample, which is related to the crack propagation time. The higher chloride concentration experienced a shorter crack nucleation time, approximately a 55% decrease from 4 to 8 wt.% Cl^-. In addition, the specimen exposed to 8 wt.% Cl^- had a higher v_{crack} by the failure with 5.27 × 10^{-9} m/s compared with the 3.25 × 10^{-9} m/s of the 4 wt.% Cl^-. The rise in the v_{crack} is related to the increase in cleavage facet surface over the microvoids/dimple surface, denoting a more brittle rupture, due to the α–phase (ferrite cleavage facets) needing less energy to crack than the γ–phase [48]. The loss in toughness (area over the stress/strain curve from the σ_y to failure) is because of the α–phase prematurely cracking with the increase in chloride content rising over the chloride threshold of the α–phase [49].

The samples strained in the CBS exhibited similar cracking behavior as the ones in the SCPS, with exception of the higher v_{crack} values and the shorter crack nucleation times for the 8 wt.% Cl^- (see Figure 8b). The higher current densities seen in the LPR monitoring coincide with the fractographic analysis, higher crack density, and greater cleavage facets surface. The embrittlement of the UNS S32205 reinforcements in the CBS is due to the reaction of the CO_2 in the solution with the water forming carbonic acid (H_2CO_3) and its later dissociation into HCO_3^- and CO_3^{2-}, enhancing the cracking susceptibility of the α–phase (see Equations (6)–(8)) [26]:

$$CO_2 + H_2O \rightarrow H_2CO_3 \quad (6)$$

$$H_2CO_3 + H_2O \leftrightarrows H^+ + HCO_3^- \quad (7)$$

$$HCO_3^- + H_2O \leftrightarrows H^+ + CO_3^{2-} \quad (8)$$

The enhancement of the acidification due to the promotion of H^+ further increases the cracking susceptibility of the α–phase, which promotes an overall increase in the anodic current density [16]. The higher current densities are responsible for the higher v_{crack}, being 8.36×10^{-9} and 1.23×10^{-8} m/s for 4 to 8 wt.% Cl^-, respectively. Comparing the SCPS and the CBS at 8 wt.% Cl^-, it can be seen that the v_{crack} at failure increased by more than 100%. This higher crack growth is related to the concentration of HCO_3^-, which is dependent on the concentrations of CO_3^{2-} and H_2CO_3 [50].

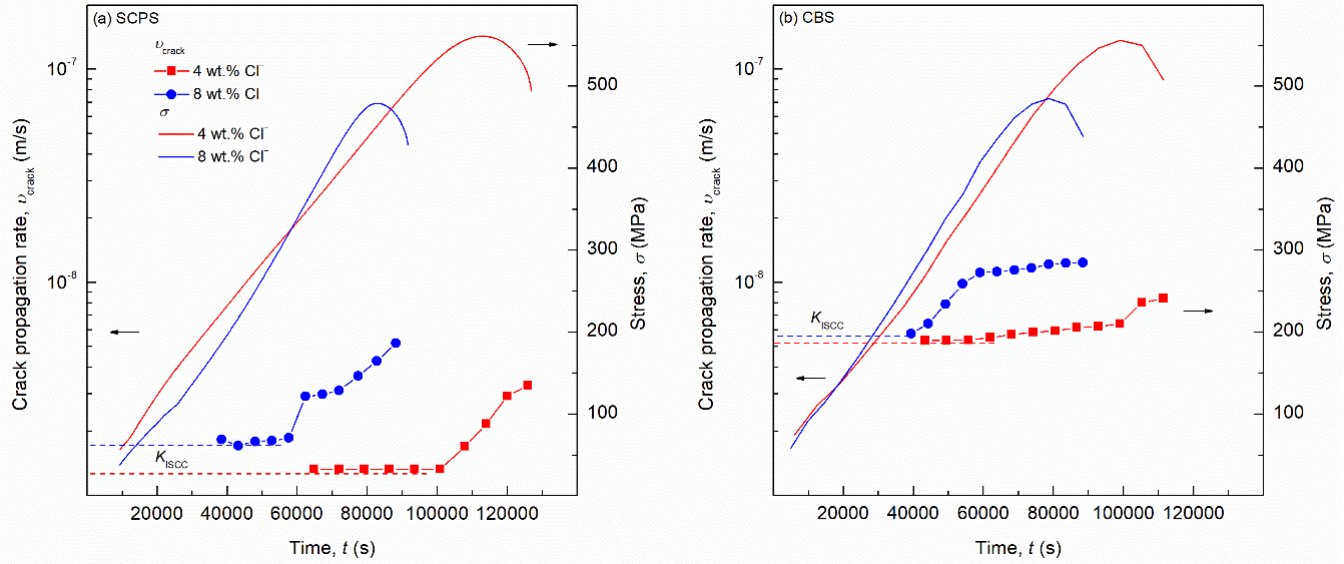

Figure 8. Crack propagation rate and stress monitoring UNS S32205 reinforcement during SSRT: (**a**) simulated concrete pore solution (SCPS, pH 12.6), and (**b**) carbonated solution (CBS, pH 9.1).

4.2. Electrochemical Impedance Spectroscopy (EIS)

After the fitting of the impedance data with the proposed EEC with two time constants (see Figure 5), the obtained values for each of the individual elements was gathered in Table 3. The R_s for all samples was between 3.01 and 4.95 Ω cm^2. The R_{film} for the samples immersed in the SCPS remained in the 10^3 Ω cm^2, slightly decreasing with applied stress, as well as with increasing chloride addition. The Y_{film} perceived more changes with the chloride addition, doubling its value with each chloride addition, where the 0 wt.% Cl^- started with 1.26×10^{-6} S cm^{-2} $s^{n,film}$, followed by 2.19 and 4.05×10^{-6} S cm^{-2} $s^{n,film}$ for 4 and 8 wt.% Cl^-, respectively. Accordingly, the corresponding n_{film} also decreased its ideality ($n < 1$) [51]. The most significant changes were seen in the second time constant $R_{ct}//CPE_{dl}$, where the values of the R_{ct} decreased one order of magnitude at the "Failure" for the 8 wt.% Cl^-, going from the average 10^5 to 10^4 Ω cm^2. While it is a decrease in one order of magnitude, it was seen in the most extreme case in both chlorides and applied stress. It is when the samples are immersed in the CBS that the change in R_{ct} becomes more relevant, starting in the 10^4 Ω cm^2 for 8 wt.% Cl^-, when the previous chloride concentrations remained in the 10^5 Ω cm^2. This coincides with the i_{corr} monitoring seen via the LPR, where the 8 wt.% Cl^- experienced the highest values. The n_{dl} values for all strained samples in the CBS had lower values than the SCPS, becoming less ideal capacitors. The electrochemical double-layer suggests a more defective layer, where electrons are easily transferred from the metal surface to the electrolyte [52].

From the *CPE* elements (CPE_{film} and CPE_{dl}), the capacitance cannot be directly measured because they are a nonideal capacitor representing a branched ladder *RC* network, [53]. In order to correct the pseudocapacitance value of the CPE_{film} and CPE_{dl} and find its effective capacitance (C_{eff}), Mansfeld and Brug equations are used to correct the pseudocapacitance values (see Equations (9) and (10)) [54,55]:

$$C_{eff,\ film} = Y_{film}\left(\omega''_m\right)^{n_{film}-1} \tag{9}$$

$$C_{eff,\ dl} = \left[Y_{dl}\left(\frac{1}{R_s} + \frac{1}{R_{ct}}\right)^{(n_{dl}-1)}\right]^{\frac{1}{n_{dl}}} \tag{10}$$

where ω''_m is the angular frequency at the maximum of the imaginary part (absolute value) of the impedance in the Nyquist plot. For the $C_{eff,film}$, the ω''_m was based on the first time constant representing the film.

From the corrected $C_{eff,film}$ values, the estimated thickness can also be obtained using Equation (11):

$$C_{eff,film} = \frac{\varepsilon_o\ \varepsilon_{film}\ A}{d} \tag{11}$$

where ε_o is the dielectric constant of the permittivity of the vacuum (8.84×10^{-14}), ε_{film} is the dielectric constant of the oxide film (a value of 15 for the passive film formed in stainless steel), A is the exposed surface area, and d is the thickness of the passive film [56,57].

The $C_{eff,film}$ and $C_{eff,dl}$ values are in the range of $\mu F/cm^2$, with the $C_{eff,film}$ ranging between 0.4 and 2.73 $\mu F/cm^2$ for the SCPS, and between 0.6 and 3.6 $\mu F/cm^2$ for the CBS, while the $C_{eff,dl}$ ranged between 0.3 and 1.1 $\mu F/cm^2$ for the SCPS, and between 0.6 and 1.6 $\mu F/cm^2$ for the CBS. With the values from the $C_{eff,film}$ and Equation (11), the thickness of the passive film was calculated to range between 33.2 and 4.8 nm.

From the impedance data, the pit-to-crack transition can also be seen by looking at the phase angle (θ) from the Bode plot [58]. As the samples strained in 8 wt.% Cl^- experienced the most brittle fracture, as well as showing the highest cracking susceptibility by electrochemical measurements, the Bode plots from both the SCPS and the CBS can be seen in Figure 9. Starting with the SCPS, the peak with the maximum θ value (θ_{max}) lays in the low-frequency region (≈1 Hz), shifting towards lower frequencies after the "Preload"; however, the θ remained unchanged in the –75° (see Figure 9a). The samples strained in the CBS experienced a decrease in the θ_{max}, which coincide in frequency range with the SCPS (≈1 Hz) (see Figure 9b). Therefore, while the θ_{max} started at a similar value (≈–77°), as the samples were strained, the θ_{max} decreased, a sign of the damage taken [58]. Furthermore, the combination of the decreasing θ_{max} with the low-frequency range indicates that the cracking process is being developed [59]. At the "Failure", the θ_{max} decreased to –60°, and the attenuation of the peak found at high frequencies denotes a deep crack [60].

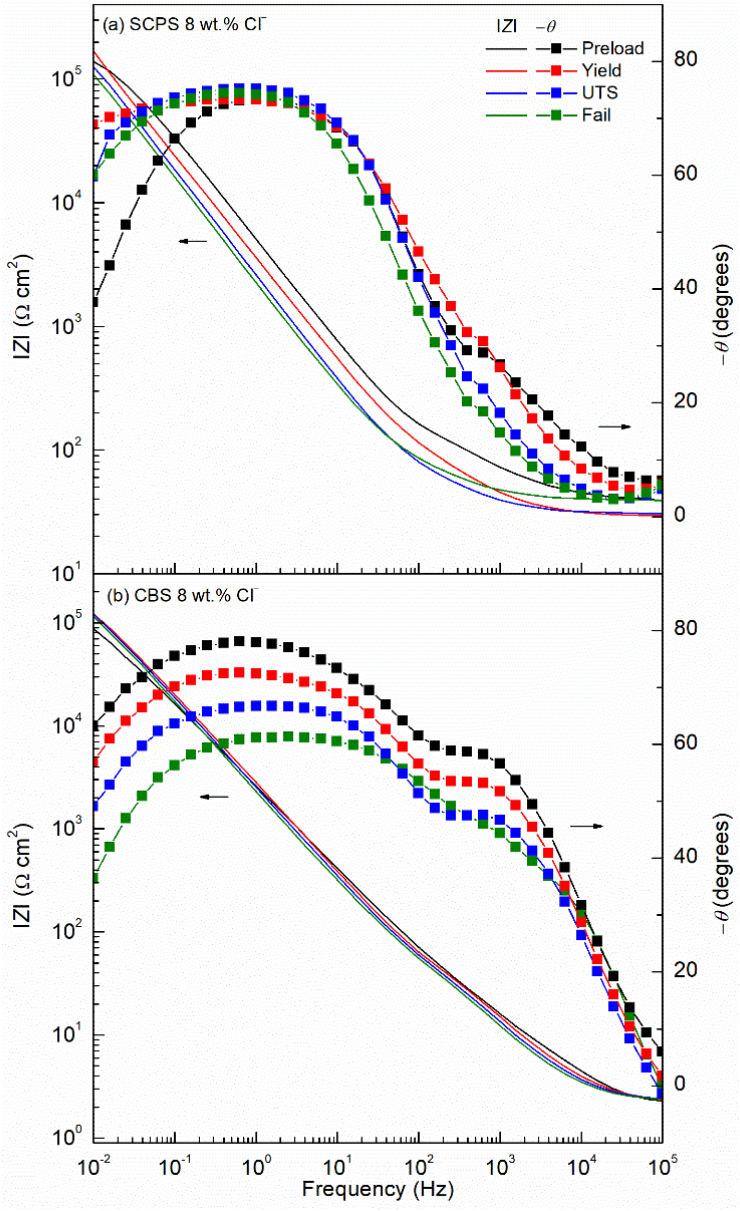

Figure 9. Bode plots of UNS S32205 reinforcement during SSRT: (**a**) simulated concrete pore solution (SCPS, pH 12.6), and (**b**) carbonated solution (CBS, pH 9.1).

4.3. Energy-Dispersive X-ray Spectroscopy (EDX)

Figure 10a shows a magnification of Figure 7i where the inclusion can be seen. This inclusion was found inside a cleavage facet, which showed higher chromium and lower nickel content, suggesting α–phase (ferrite cleavage facet) [49]. Performing an EDX analysis on the inclusion, it was confirmed that it was a TiN nonmetallic inclusion (NMI) (see Figure 10b) [61,62]. This type of TiN NMI has been seen to promote higher corrosion susceptibility in duplex stainless steel, leading in some cases to the promotion of TG-SCC [63,64]. As can be seen on the EDX spectra, the highest peaks correspond with Ti and N; nevertheless, some minor traces of Fe and Cr from the substrate of the ferrite cleavage facet were also seen [65–67].

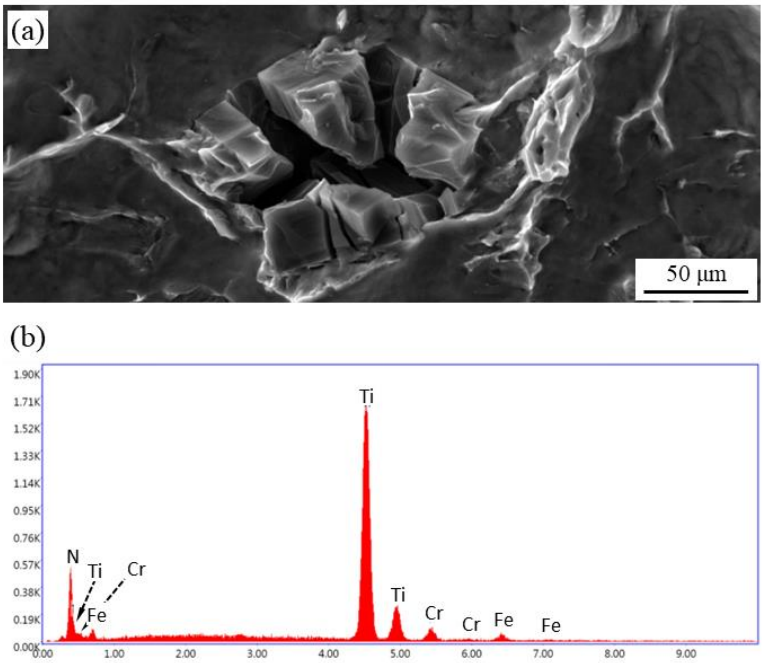

Figure 10. EDX analysis of Ti-based nonmetallic inclusion in UNS S32205 reinforcement after failure immersed in carbonated solution (CBS, pH 9.1) contaminated with 8 wt.% Cl^-: (**a**) SEM micrograph ×7600, and (**b**) EDX spectrum.

The TiN NMI has been proven to be more susceptible to cracking than the matrix, which in the case of UNS S32205 was the ferrite cleavage facet, thus acting as crack nucleation sites where brittle fracture is developed [49]. The TG-SCC behavior seen in both the SCPS and the CBS, with the predominant failure by the ferrite cleavage facet formation, is the consequence of the cracking of the TiN NMI. Near these sites, neither ductile fracture nor ductile overload fracture was seen (absence of microvoids and coalescence of dimples), where the dominant fracture mode is brittle.

5. Conclusions

In this work, the influence of the carbonation process and the chloride concentration on the SCC mechanism of UNS S32205 reinforcement was studied. The main conclusions can be drawn as follows:

The monitoring of the i_{corr} via LPR coincided with the findings observed by EIS analysis, where the CBS experienced higher i_{corr} and lower R_{ct} values, a sign of a more susceptible alloy.

The increase in chloride content shifted the ductile fracture with microvoids and coalescence of dimples to brittle fracture with the development of a greater surface with cleavage facets. The change in carbonation enhanced the brittle fracture, reducing the ductile and ductile overload areas. The α–phase, majorly present in the ferrite cleavage facets, had the highest cracking susceptibility and was the main reason for the brittle fracture.

The v_{crack} of the UNS S32205 specimens exposed to SCPS had a maximum value of 5.27×10^{-9} m/s by the failure of the sample in 8 wt.% Cl^-, which increased over 100% for the same conditions for the CBS reaching 1.23×10^{-8} m/s. The enhanced acidification due to the formation of carbonic acid and its later dissociation was the reason for the higher cracking susceptibility of the ferrite cleavage facet, increasing accordingly the v_{crack} and promoting a more severe brittle fracture.

The pit-to-crack transition was seen by the decrease in the θ_{max} for the CBS with 8 wt.% Cl^-, decreasing from $\approx -77°$ up to $\approx -60°$ by the failure of the sample. In addition, the θ_{max} was developed at low frequencies (≈1 Hz), corresponding to the cracking process.

The TiN NMI inside the ferrite cleavage facets was the cause of the faster crack nucleation, promoting a more brittle fracture. The increase in aggressiveness of the electrolyte with the CBS and the chloride addition enhanced the cracking process, promoting the brittle rupture of a higher number of TiN NMI.

Author Contributions: Conceptualization, D.M.B.; Methodology, U.M. and D.M.B.; Experimental design, U.M. and D.M.B.; Data analysis, U.M. and D.M.B.; Resources, D.M.B.; Writing—original draft preparation, U.M. and D.M.B.; Writing—review and editing, U.M. and D.M.B.; Visualization, D.M.B.; Supervision, D.M.B.; Project administration, D.M.B.; Funding acquisition, D.M.B. All authors have read and agreed to the published version of the manuscript.

Funding: This research was funded by Firestone Research Grant 639430, and The University of Akron Fellowships FRC-207160 and FRC-207865.

Institutional Review Board Statement: Not applicable.

Informed Consent Statement: Not applicable.

Data Availability Statement: The raw/processed data required to reproduce these findings cannot be shared at this time as the data also form part of an ongoing study.

Acknowledgments: The authors acknowledge the technical support and facilities from The National Center for Education and Research on Corrosion and Materials Performance (NCERCAMP-UA), the College of Engineering and Polymer Science, and The University of Akron.

Conflicts of Interest: The authors declare no conflict of interest.

References

1. de Farias Azevedo, C.R.; Boschetti Pereira, H.; Wolynec, S.; Padilha, A.F. An overview of the recurrent failures of duplex stainless steels. *Eng. Fail. Anal.* **2019**, *97*, 161–188. [CrossRef]
2. Gunn, R. *Duplex Stainless Steels: Microstructure, Properties and Applications*; Woodhead Publishing: Sawston, UK, 1997; ISBN 1855733188.
3. Yang, X.; Shao, J.; Liu, Z.; Zhang, D.; Cui, L.; Du, C.; Li, X. Stress-assisted microbiologically influenced corrosion mechanism of 2205 duplex stainless steel caused by sulfate-reducing bacteria. *Corros. Sci.* **2020**, *173*, 108746. [CrossRef]
4. Tsai, W.T.; Chen, M.S. Stress corrosion cracking behavior of 2205 duplex stainless steel in concentrated NaCl solution. *Corros. Sci.* **2000**, *42*, 545–559. [CrossRef]
5. Biezma, M.V.; Martin, U.; Linhardt, P.; Ress, J.; Rodríguez, C.; Bastidas, D.M. Non-destructive techniques for the detection of sigma phase in duplex stainless steel: A comprehensive review. *Eng. Fail. Anal.* **2021**, *122*, 105227. [CrossRef]
6. Okayasu, M.; Fujiwara, T. Effects of microstructural characteristics on the hydrogen embrittlement characteristics of austenitic, ferritic, and γ–α duplex stainless steels. *Mater. Sci. Eng. A* **2021**, *807*, 140851. [CrossRef]
7. Örnek, C.; Davut, K.; Kocabaş, M.; Bayatlı, A.; Ürgen, M. Understanding corrosion morphology of duplex stainless steel wire in chloride electrolyte. *Corros. Mater. Degrad.* **2021**, *2*, 397–411. [CrossRef]
8. Tsai, W.-T.T.; Chou, S.-L.L. Environmentally assisted cracking behavior of duplex stainless steel in concentrated sodium chloride solution. *Corros. Sci.* **2000**, *42*, 1741–1762. [CrossRef]
9. Sofia Hazarabedian, M.; Viereckl, A.; Quadir, Z.; Leadbeater, G.; Golovanevskiy, V.; Erdal, S.; Georgeson, P.; Iannuzzi, M.; So, M.; Viereckl, A.; et al. Hydrogen-induced stress cracking of swaged super duplex stainless steel subsea components. *Corrosion* **2019**, *75*, 824–838. [CrossRef]
10. Örnek, C.; Léonard, F.; McDonald, S.A.; Prajapati, A.; Withers, P.J.; Engelberg, D.L. Time-dependent in situ measurement of atmospheric corrosion rates of duplex stainless steel wires. *NPJ Mater. Degrad.* **2018**, *2*, 10. [CrossRef]
11. Reccagni, P.; Guilherme, L.H.; Lu, Q.; Gittos, M.F.; Engelberg, D.L. Reduction of austenite-ferrite galvanic activity in the heat-affected zone of a Gleeble-simulated grade 2205 duplex stainless steel weld. *Corros. Sci.* **2019**, *161*, 108198. [CrossRef]
12. Luu, W.; Liu, P.; Wu, J. Hydrogen transport and degradation of a commercial duplex stainless steel. *Corros. Sci.* **2002**, *44*, 1783–1791. [CrossRef]
13. Martínez-Pañeda, E.; Harris, Z.D.; Fuentes-Alonso, S.; Scully, J.R.; Burns, J.T. On the suitability of slow strain rate tensile testing for assessing hydrogen embrittlement susceptibility. *Corros. Sci.* **2020**, *163*, 108291. [CrossRef]
14. Yousefi, A.; Itoh, G. Tensile properties of an electrolytically hydrogen charged duplex stainless steel affected by strain rate. *ISIJ Int.* **2018**, *58*, 561–565. [CrossRef]
15. Martin, U.; Bastidas, D.M. Stress corrosion cracking failure analysis of aisi 1018 carbon steel reinforcing bars in carbonated and chloride contaminated environment. *Eng. Fail. Anal.* **2023**, *146*, 107159. [CrossRef]
16. Liu, Z.Y.; Dong, C.F.; Li, X.G.; Zhi, Q.; Cheng, Y.F. Stress corrosion cracking of 2205 duplex stainless steel in H_2S–CO_2 environment. *J. Mater. Sci.* **2009**, *44*, 4228–4234. [CrossRef]

17. Bertolini, L.; Bolzoni, F.; Pastore, T.; Pedeferri, P. Behaviour of stainless steel in simulated concrete pore solution. *Br. Corros. J.* **1996**, *31*, 218–222. [CrossRef]
18. Moser, R.D.; Singh, P.M.; Kahn, L.F.; Kurtis, K.E. Chloride-induced corrosion resistance of high-strength stainless steels in simulated alkaline and carbonated concrete pore solutions. *Corros. Sci.* **2012**, *57*, 241–253. [CrossRef]
19. *ASTM G129-21*; Standard Practice for Slow Strain Rate Testing to Evaluate the Susceptibility of Metallic Materials to Environmentally Assisted Cracking. ASTM International: West Conshohocken, PA, USA, 2021. [CrossRef]
20. Hurley, M.F.; Scully, J.R. Threshold chloride concentrations of selected corrosion-resistant rebar materials compared to carbon steel. *Corrosion* **2006**, *62*, 892–904. [CrossRef]
21. *ASTM G59-97*; Standard Test Method for Conducting Potentiodynamic Polarization Resistance Measurements. ASTM International: West Conshohocken, PA, USA, 2020. [CrossRef]
22. Sandim, M.J.R.; Souza Filho, I.R.; Mota, C.F.G.S.; Zilnyk, K.D.; Sandim, H.R.Z. Microstructural and magnetic characterization of a lean duplex steel: Strain-induced martensite formation and austenite reversion. *J. Magn. Magn. Mater.* **2021**, *517*, 167370. [CrossRef]
23. Knyazeva, M.; Pohl, M. Duplex Steels: Part I: Genesis, Formation, Structure. *Metallogr. Microstruct. Anal.* **2013**, *2*, 113–121. [CrossRef]
24. Hammood, A.S. Biomineralization of 2304 duplex stainless steel with surface modification by electrophoretic deposition. *J. Appl. Biomater. Funct. Mater.* **2020**, *18*, 228080001989621. [CrossRef]
25. Guo, L.; Hua, G.; Yang, B.; Lu, H.; Qiao, L.; Yan, X.; Li, D. Electron work functions of ferrite and austenite phases in a duplex stainless steel and their adhesive forces with AFM silicon probe. *Sci. Rep.* **2016**, *6*, 20660. [CrossRef]
26. Wang, X.; Fu, H.; Du, D.; Zhou, Z.; Zhang, A.; Su, C.; Ma, K. The comparison of pKa determination between carbonic acid and formic acid and its application to prediction of the hydration numbers. *Chem. Phys. Lett.* **2008**, *460*, 339–342. [CrossRef]
27. Davies, D.H.; Burstein, G.T. The effects of bicarbonate on the corrosion and passivation of iron. *Corrosion* **1980**, *36*, 416–422. [CrossRef]
28. Stefánsson, A. Iron(III) hydrolysis and solubility at 25 °C. *Environ. Sci. Technol.* **2007**, *41*, 6117–6123. [CrossRef]
29. Singley, J.E.; Black, A.P. Hydrolysis products of iron (III). *J. Am. Water Work. Assoc.* **1967**, *59*, 1549–1564. [CrossRef]
30. Briz, E.; Biezma, M.V.; Bastidas, D.M. Stress corrosion cracking of new 2001 lean–duplex stainless steel reinforcements in chloride contained concrete pore solution: An electrochemical study. *Constr. Build. Mater.* **2018**, *192*, 1–8. [CrossRef]
31. Babu, U.R.; Kondraivendhan, B. Effect of IR drop on reinforced concrete corrosion measurements. *IOP Conf. Ser. Mater. Sci. Eng.* **2020**, *829*, 012015. [CrossRef]
32. Cui, Z.; Wang, L.; Ni, H.; Hao, W.; Man, C.; Chen, S.; Wang, X.; Liu, Z.; Li, X. Influence of temperature on the electrochemical and passivation behavior of 2507 super duplex stainless steel in simulated desulfurized flue gas condensates. *Corros. Sci.* **2017**, *118*, 31–48. [CrossRef]
33. Bastidas, D.M.; Fernández-Jiménez, A.; Palomo, A.; González, J.A. A study on the passive state stability of steel embedded in activated fly ash mortars. *Corros. Sci.* **2008**, *50*, 1058–1065. [CrossRef]
34. Ohta, K.; Ishida, H. Comparison among several numerical integration methods for Kramers-Kronig transformation. *Appl. Spectrosc.* **1988**, *42*, 952–957. [CrossRef]
35. Ress, J.; Martin, U.; Bosch, J.; Bastidas, D.M. pH-Triggered release of NaNO2 corrosion inhibitors from novel colophony microcapsules in simulated concrete pore solution. *ACS Appl. Mater. Interfaces* **2020**, *12*, 46686–46700. [CrossRef] [PubMed]
36. Cojocaru, E.M.; Raducanu, D.; Vintila, A.N.; Alturaihi, S.S.; Serban, N.; Berbecaru, A.C.; Cojocaru, V.D. Influence of ageing treatment on microstructural and mechanical properties of a solution treated UNS S32750/EN 1.4410/F53 super duplex stainless steel (SDSS) alloy. *J. Mater. Res. Technol.* **2020**, *9*, 8592–8605. [CrossRef]
37. Hilders, O.; Zambrano, N. The effect of aging on impact toughness and fracture surface fractal dimension in SAF 2507 super duplex stainless steel. *J. Microsc. Ultrastruct.* **2014**, *2*, 236–244. [CrossRef]
38. Li, S.; Wang, Y.; Wang, X. In situ observation of the deformation and fracture behaviors of long-term thermally aged cast duplex stainless steels. *Metals* **2019**, *9*, 258. [CrossRef]
39. Liu, G.; Li, S.-L.; Zhang, H.-L.; Wang, X.-T.; Wang, Y.-L. Characterization of impact deformation behavior of a thermally aged duplex stainless steel by EBSD. *Acta Metall. Sin. English Lett.* **2018**, *31*, 798–806. [CrossRef]
40. Topolska, S.; Labanowski, J. Impact-toughness investigations of duplex stainless steels. *Mater. Tehnol.* **2015**, *49*, 481–486. [CrossRef]
41. Martin Diaz, U.; Birbilis, N.; Macdonald, D.D.; Bastidas, D.M. Passivity breakdown and crack propagation mechanisms of lean duplex (UNS S32001) stainless steel reinforcement in high alkaline solution under stress corrosion cracking. *Corrosion* **2023**, *79*, 4229. [CrossRef]
42. Park, H.; Moon, B.; Moon, Y.; Kang, N. Hydrogen stress cracking behaviour in dissimilar welded joints of duplex stainless steel and carbon steel. *Metals* **2021**, *11*, 1039. [CrossRef]
43. MacDonald, D.D.; Urquidi-MacDonald, M. A coupled environment model for stress corrosion cracking in sensitized type 304 stainless steel in LWR environments. *Corros. Sci.* **1991**, *32*, 51–81. [CrossRef]
44. Filippi, S.; Lazzarin, P.; Tovo, R. Developments of some explicit formulas useful to describe elastic stress fields ahead of notches in plates. *Int. J. Solids Struct.* **2002**, *39*, 4543–4565. [CrossRef]
45. Lazzarin, P.; Filippi, S. A generalized stress intensity factor to be applied to rounded V-shaped notches. *Int. J. Solids Struct.* **2006**, *43*, 2461–2478. [CrossRef]

46. Weng, S.; Huang, Y.; Lin, S.; Xuan, F. Stress corrosion crack propagation affected by microstructures for nuclear steam turbine rotor steels in the simulated environment. *J. Mater. Res. Technol.* **2022**, *17*, 725–742. [CrossRef]
47. Galakhova, A.; Prattes, K.; Mori, G. High-temperature high-pressure SCC testing of corrosion-resistant alloys. *Mater. Corros.* **2021**, *72*, 1831–1842. [CrossRef]
48. Alwin, B.; Lakshminarayanan, A.K.; Vasudevan, M.; Vasantharaja, P. Assessment of stress corrosion cracking resistance of activated tungsten inert gas-welded duplex stainless steel joints. *J. Mater. Eng. Perform.* **2017**, *26*, 5825–5836. [CrossRef]
49. Liang, X.Z.; Zhao, G.-H.; Dodge, M.F.; Lee, T.L.; Dong, H.B.; Rivera-Díaz-del-Castillo, P.E.J. Hydrogen embrittlement in super duplex stainless steels. *Materialia* **2020**, *9*, 100524. [CrossRef]
50. Parkins, R.N.; Zhou, S. The stress corrosion cracking of C-Mn steel in CO2-HCO3 −CO32 − solutions. II: Electrochemical and other data. *Corros. Sci.* **1997**, *39*, 175–191. [CrossRef]
51. Martin, U.; Bosch, J.; Ress, J.; Bastidas, D.M. Long-term stability and electronic properties of passive film of lean-duplex stainless steel reinforcements in chloride containing mortar. *Constr. Build. Mater.* **2021**, *291*, 123319. [CrossRef]
52. Montemor, M.; Simões, A.M.; Ferreira, M.G. Chloride-induced corrosion on reinforcing steel: From the fundamentals to the monitoring techniques. *Cem. Concr. Compos.* **2003**, *25*, 491–502. [CrossRef]
53. Bastidas, D.M. Interpretation of impedance data for porous electrodes and diffusion processes. *Corrosion* **2007**, *63*, 515–521. [CrossRef]
54. Hsu, C.H.; Mansfeld, F. Technical Note: Concerning the conversion of the constant phase element parameter Y0 into a capacitance. *Corrosion* **2001**, *57*, 747–748. [CrossRef]
55. Brug, G.J.; van den Eeden, A.L.G.; Sluyters-Rehbach, M.; Sluyters, J.H. The analysis of electrode impedances complicated by the presence of a constant phase element. *J. Electroanal. Chem. Interfacial Electrochem.* **1984**, *176*, 275–295. [CrossRef]
56. Hakiki, N.B.; Boudin, S.; Rondot, B.; Da Cunha Belo, M. The electronic structure of passive films formed on stainless steels. *Corros. Sci.* **1995**, *37*, 1809–1822. [CrossRef]
57. Fajardo, S.; Bastidas, D.M.; Criado, M.; Bastidas, J.M. Electrochemical study on the corrosion behaviour of a new low-nickel stainless steel in carbonated alkaline solution in the presence of chlorides. *Electrochim. Acta* **2014**, *129*, 160–170. [CrossRef]
58. Bosch, R.-W. Electrochemical impedance spectroscopy for the detection of stress corrosion cracks in aqueous corrosion systems at ambient and high temperature. *Corros. Sci.* **2005**, *47*, 125–143. [CrossRef]
59. Lou, X.; Singh, P.M. Phase angle analysis for stress corrosion cracking of carbon steel in fuel-grade ethanol: Experiments and simulation. *Electrochim. Acta* **2011**, *56*, 1835–1847. [CrossRef]
60. Naskar, A.; Bhattacharyya, M.; Raja, K.S.; Charit, I.; Darsell, J.; Jana, S. Pitting behavior of friction stir repair-welded 304L stainless steel in 3.5% NaCl solution at room temperature: Role of grain and defect structures. *SN Appl. Sci.* **2020**, *2*, 2164. [CrossRef]
61. Fedorov, A.; Zhitenev, A.; Karasev, V.; Alkhimenko, A.; Kovalev, P. Development of a methodology for the quality management of duplex stainless steels. *Materials* **2022**, *15*, 6008. [CrossRef]
62. Ma, Q.; Wu, C.; Cheng, G.; Li, F. Characteristic and formation mechanism of inclusions in 2205 duplex stainless steel containing rare earth elements. *Mater. Today Proc.* **2015**, *2*, S300–S305. [CrossRef]
63. Todoshchenko, O.; Yagodzinskyy, Y.; Yagodzinska, V.; Saukkonen, T.; Hänninen, H. Hydrogen effects on fracture of high-strength steels with different micro-alloying. *Corros. Rev.* **2015**, *33*, 515–527. [CrossRef]
64. Liu, P.; Zhang, Q.; Watanabe, Y.; Shoji, T.; Cao, F. A critical review of the recent advances in inclusion-triggered localized corrosion in steel. *NPJ Mater. Degrad.* **2022**, *6*, 81. [CrossRef]
65. Kiviö, M.; Holappa, L.; Iung, T. Addition of dispersoid titanium oxide inclusions in steel and their influence on grain refinement. *Metall. Mater. Trans. B* **2010**, *41*, 1194–1204. [CrossRef]
66. Rezaei, H.A.; Ghazani, M.S.; Eghbali, B. Effect of post deformation annealing on the microstructure and mechanical properties of cold rolled AISI 321 austenitic stainless steel. *Mater. Sci. Eng. A* **2018**, *736*, 364–374. [CrossRef]
67. Ghazani, M.S.; Eghbali, B. Characterization of the hot deformation microstructure of AISI 321 austenitic stainless steel. *Mater. Sci. Eng. A* **2018**, *730*, 380–390. [CrossRef]